NIST Author Manuscript

NIST Author Manuscript

NIST Author Manuscript

Facile route to bulk ultrafine-grain steels for high strength and ductility

Junheng Gao[1], **Suihe Jiang**[2,*], **Huairuo Zhang**[3,4,*], **Yuhe Huang**[1], **Dikai Guan**[1], **Yidong Xu**[1], **Shaokang Guan**[5], **Leonid A. Bendersky**[4], **Albert V. Davydov**[4], **Yuan Wu**[2], **Huihui Zhu**[2], **Yandong Wang**[2], **Zhaoping Lu**[2,*], **W. Mark Rainforth**[1,*]

[1]Department of Materials Science and Engineering, The University of Sheffield, S1 3JD, UK

[2]Beijing Advanced Innovation Centre for Materials Genome Engineering, State Key Laboratory for Advanced Metals and Materials, University of Science and Technology Beijing, Beijing, 100083, China

[3]Theiss Research, Inc., La Jolla, CA 92037, USA

[4]Materials Science and Engineering Division, National Institute of Standards and Technology (NIST), Gaithersburg, MD 20899, USA

[5]School of Materials Science and Engineering, Zhengzhou University, Zhengzhou, 450002, China

Abstract

Steels with sub-micron grain sizes usually possess high toughness and strength, which makes them promising for light-weighting technologies and energy saving strategies. To date, industrial fabrication of UFG (ultrafine-grained) alloys, which generally relies on the manipulation of diffusional phase transformation, is limited to steels with austenite to ferrite transformation[1–3]. Moreover, the limited work hardening and uniform elongation of these UFG steels[1,4,5] hinder their widespread application. Herein, we report the easy mass production of UFG structures in a typical Fe-22Mn-0.6C TWIP (twinning-induced plasticity) steel via minor Cu alloying and manipulating the recrystallization process by intragranular nanoprecipitation (within 0.5 min) of a coherent disordered Cu-rich phase. The timely rapid and copious nanoprecipitation not only prevents the

Publisher's Disclaimer: Disclaimer: Certain commercial equipment, instruments, or materials are identified in this paper to foster understanding. Such identification does not imply recommendation or endorsement by the National Institute of Standards and Technology, nor does it imply that the materials or equipment identified are necessarily the best available for the purpose.

Data availability
The data that support the findings of this study are available from the corresponding authors upon reasonable request.

growth of the freshly recrystallized sub-micron grains, but also substantially enhances thermal stability of the obtained UFG structure due to their strong and sustainable Zener pinning effect. Importantly, the precipitates exhibit weak interactions with dislocations under loading due to their full coherency and disordered nature. Consequently, a fully-recrystallized UFG structure with 800 ± 400 nm grain size was developed without the introduction of any detrimental lattice defects such as brittle particles and segregated boundaries. The resultant mechanical performance is strikingly enhanced, i.e., the yield strength of the UFG steel was doubled (to ~ 710 MPa), with simultaneously large uniform ductility of 45 % and high tensile strength (~ 2000 MPa). The current grain refinement concept can be extended to other alloy systems, and the manufacturing processes can also be readily applied to existing industrial production lines.

Mechanical performance

To fabricate bulk UFG steels with both high strength and high ductility by a simple manufacturing route, a typical Fe-22Mn-0.6C TWIP steel without solid phase transformation was alloyed with 3 and 4 wt. % Cu (weight per cent), which enables rapid and sufficient nanoprecipitation at the recrystallization temperature (see Methods for composition design). Hereafter, the Fe-22Mn-0.6C and the Cu-doped Fe-22Mn-0.6C-3Cu and Fe-22Mn-0.6C-4Cu steels are referred to as 0Cu, 3Cu, and 4Cu, respectively. Fig. 1a shows the true tensile stress-strain curves of the three alloys annealed at 760 °C for 5 and 20 min. A significant increase in the yield strength and ultimate tensile strength (σ_{uts}) was observed in the Cu-doped steels. Specifically, the yield strength is nearly doubled from 365 ± 18 MPa for 0Cu to 710 ± 26 MPa for 4Cu after 5 min annealing, whereas 4Cu retains a comparable ductility with coarse-grained 0Cu (Fig.1a and Extended Data Fig. 1). Moreover, the Cu-doped steels exhibit an ultrahigh strain hardening rate (~ 2900 MPa, Fig. 1b), even higher than that (~ 2500 MPa) of coarse-grained 0Cu, which is responsible for the high σ_{uts} (1976 ± 32 MPa) and large uniform elongation. The large uniform elongation of 45 % for 4Cu is highlighted in the normalized strain hardening curve (inset of Fig. 1a). This behaviour is in contrast to the rapid loss of work hardening capability with the decrease of grain sizes in traditional UFG alloy[4,5]. More importantly, an enhanced yield strength (620 ± 21 MPa; dashed blue curve in Fig. 1a) and large ductility were also observed in the 4Cu annealed at 760 °C for 20 min, suggesting the high stability of the Cu-alloyed microstructure. Yield strength is critical for anti-intrusion beams of vehicles while tensile strength and uniform ductility are essential properties responsible for light-weighting, press-forming capability and energy absorption capability for improving crashworthiness during collisions. Thus, we compare yield strength versus the product of σ_{uts} and uniform EL (elongation) of the Cu-alloyed steels in Fig. 1c, with those of other high-performance alloys reported in literature[6–23]. The Cu-doped TWIP steels exhibit a unique combination of higher yield strength and larger values of $\sigma_{uts} \times$ uniform EL (i.e., 71 GPa % for 4Cu), even in comparison with the UFG TWIP steels fabricated by complicated processes, i.e., flash annealing[23] or repeated cold rolling and annealing[15], demonstrating the advantages of the current grain refinement strategy in simultaneously enhancing yield strength and toughness.

Microstructure and thermal stability

Fig. 2a and b display a synchrotron high-energy X-ray diffraction (XRD) pattern and an electron back-scattering diffraction (EBSD) map of 4Cu annealed at 760 °C for 5 min revealing a single-phase fully recrystallized fcc (face-centred cubic) structure with a fine grain size of 800 ± 400 nm. Further analysis with annular dark-field scanning transmission electron microscopy (ADF-STEM) in Fig. 2c revealed the presence of nanoprecipitates (bright particles) with a high number density and uniform intragranular distribution. The energy-dispersive spectroscopy spectrum-imaging (EDS-SI) image (inset of Fig. 2c) from the marked region confirms these nanoprecipitates are enriched in Cu. The selected area electron diffraction (SAED) pattern (Extended Data Fig. 2a) taken along the $[110]_{fcc}$ zone axis and the atomic resolution ADF-STEM image (Fig. 2d) show that the precipitates (bright contrast) do not exhibit extra periodicity to the fcc matrix, confirming its disordered fcc nature. Moreover, these precipitates exhibit a diffuse, fully coherent, interface with the matrix (Fig. 2d), which is responsible for their homogeneous distribution[24]. Note that a UFG structure (900 ± 400 nm) was also obtained in 3Cu, whilst the grain size of 0Cu reaches 2.2 ± 1.1 μm (Extended Data Fig. 2b, c), suggesting the critical role of Cu addition on the grain refinement and property enhancement.

Fig.2e shows the reconstruction from one APT (Atom probe tomography) dataset for 4Cu, revealing that the number density of the Cu-rich nanoprecipitates within grains is ~ 4.6×10^{23} m^{-3} with a diameter of 5.6 ± 2.5 nm. Precipitate free zones (~ 50 nm in width) adjacent to the grain boundaries were observed, indicating that the grain growth is governed by thermal stability of the nanoprecipitates. The proximity histogram in Fig. 2f reveals that the Cu content of the nanoprecipitates is 84 ± 6 at %. The 1D concentration profile (Fig. 2g) of a cylindrical region across the grain boundary demonstrates that, except for slight C segregation[25], no Cu and Mn segregation at grain boundaries occurred. Therefore, in contrast to the conventional stabilization strategies (e.g., boundary segregation and precipitation), the current approach did not introduce any excess defects at grain boundaries, which is beneficial for ductility.

The thermal stability of UFG alloys determines the processing window of manufacturing, e.g., the width of annealing temperature and time[26]. Thus, we evaluated the thermal stability of 0Cu, UFG 3Cu and 4Cu over a wide annealing temperature span (730 to 910 °C) and time range (5 to 60 min) (Fig. 3 and Extended Data Fig. 3). The grain size of 0Cu increases rapidly with annealing temperature. In contrast, the UFG microstructures of the Cu-doped steels can be retained over a wide temperature range. Interestingly, the actual stability of these Cu-adopted steels varies with the Cu content, which corresponds well to the Cu solubility in austenite at different temperatures (inset of Fig.3a). For 4Cu, the UFG structure is stable up to 910°C, that is 0.64 T_m (T_m, the melting point, is about 1430°C), demonstrating a broad temperature processing window of >150 °C(Fig. 3a and Extended Data Fig. 3). This trend is profoundly distinguished from what was reported previously in other UFG alloys[27-29], where rapid grain growth occurs when the annealing temperature approaches 0.3T_m. Furthermore, with an extension of annealing time from 5 to 60 min at 760 °C, limited grain growth was observed in 4Cu (i.e., from 0.8 to 1.3 μm) whilst grains

grow significantly from 2.1 to 5.7 μm for 0Cu (Fig. 3b and Extended Data Fig. 3), further manifesting the outstanding thermal stability of the currently produced UFG steels.

Grain refinement mechanism

To uncover the grain refinement mechanism, we studied annealing effects in 4Cu by EBSD, annular bright-field (ABF) STEM and APT techniques (Fig. 4 and Extended Data Fig. 4). Fig. 4a shows that after 0.5 min annealing, recrystallization occurred extensively. With extension of the annealing time to 1 and 2 min, the recrystallized volume fraction increases to 76 and 95% while the grain size enlarges to 300 ± 150 and 500 ± 200 nm, respectively (Fig. 4b and Extended Data Fig. 4a–d). In addition, Cu-rich clusters with an average diameter of 2.6 nm and a number density of 1.6×10^{24} m^{-3} formed immediately after 0.5 min annealing (Fig. 4a), and, as the annealing time was extended to 1 and 2 min, the average precipitate size increases slightly to 3.7 and 4.5 nm, whilst the number density decreases to 8.8×10^{23} and 6.1×10^{23} m^{-3}, respectively (Fig. 4a, b and Extended Data Fig. 4e). Accompanying the size growth, the Cu content in these precipitates also increases from 56 ± 4 to 76 ± 5 at % in going from 0.5 to 2min, as shown by the proximity histograms in Fig. 4a and b (see details regarding particle composition correction in Methods and Extended Data Fig. 5). The gradual enrichment of Cu in the precipitates with growth suggests that the formation of these disordered precipitates is dominated by a simple solute-enrichment process, which contributes to the rapid nanoprecipitation, as discussed below.

To further unravel the interrelationship between recrystallization, nanoprecipitation and mechanism responsible for the high thermal stability of 4Cu, we compared the evolution of the driving pressure for recrystallization (P_r, the stored energy of the un-recrystallized grains), Zener pinning pressure (P_z, resulted from the formation of excess incoherent interfaces owing to the interaction between the coherent nanoprecipitates and migrating grain boundaries), and driving pressure for grain growth (P_g, originated from the decrease of total grain boundary energy) as a function of annealing time at 760 °C (Fig. 4c). Although the overall dislocation density decreases greatly with annealing, nevertheless, the local dislocation density of un-recrystallized grains only decreases slightly, leading to a constant P_r (Fig. 4c). Thus, P_r (~28.6 MPa, see Methods), is constantly higher than P_z (Fig. 4c), resulting in a quick recrystallization process (i.e., after ~ 2–3 min annealing). However, due to the rapid and copious precipitation at the onset of annealing, the P_z increases rapidly and immediately exceeds P_g after 1 min annealing, suggesting that these freshly recrystallized sub-micro grains were stabilized right after recrystallization. When the annealing extends from 1 to 5 min, the precipitates grow slightly from 3.7 to 5.6 nm, and P_z peaks at around 5 min (Fig. 4c), whilst P_g decreases gradually. When the annealing time exceeds 5 min, nanoprecipitation develops into the capillary-driving coarsening stage which generally exhibits slow kinetics due to the low driving force and long-range diffusion character. As a result, P_z is inevitably decreased but still much higher than P_g. Consequently, the UFG structure is continuously stabilized by Zener pinning (Fig. 4d, e).

It should be noted that the pinning effect actually stems from the precipitates adjacent to grain boundaries. However, the capillary-driven growth of the precipitates would unavoidably increase the space between precipitates and boundaries. As the grain boundaries

of the sub-micron grains are highly mobile, they would quickly migrate towards these precipitate-free regions until they interact with new internal nanoprecipitates where the pinning reestablishes (Fig. 4d, e). A precipitate-free space was then left behind the migrating boundary, and the small width of the precipitate-free space (~50 nm) (Fig. 2e and Fig. 4d) indicates a substantially retarded grain growth rate. Therefore, once the boundaries are pinned by nanoprecipitates, coarsening of the nanoprecipitates, which is a much slower long-range diffusion process[30], then governs the grain growth process. In conjunction with the low-misfit (0.11%, see Methods), fully coherent interfaces which significantly lowers the driving force for precipitate coarsening, the intrinsically unstable UFG grains are then continuously stabilized by the stable nanoprecipitates. The HR-TEM (high resolution) image (Fig. 4f) shows that the precipitate at a grain boundary is coherent with the shrinking grain, confirming that the strong Zener pinning effect results from the intragranular nanoprecipitates, instead of grain boundary precipitation.

The above results manifest the importance of the rapid precipitation and high stability of the copious nanoprecipitates on grain refinement. The reasons for the rapid precipitation are threefold. One is the fast kinetics resulting from the high annealing temperature, as compared with that of other high-Mn steels[31,32] (~550 °C). The second is the minimized nucleation barrier resulting from the fully coherent interfaces[24]. Additionally, the disordered nature renders the precipitation a continuous Cu localized enrichment process (Fig. 4a, b), which reduces the incubation time of nuclei in comparison with that of intermetallic precipitates that require localized enrichment of at least two elements with a strict stoichiometric ratio. Thirdly, the positive mixing enthalpy between Cu and Fe (13 kJ/mol)[33] suggests that atomic scale Cu-rich clusters would exist in the melt, which also facilitates fast precipitation.

Plastic deformation mechanism

Compared with the 0Cu annealed at 760 °C for 5 min (Fig. 1a), the total increment of the yield strength for 4Cu is 345 MPa. As expected, the calculation (see Methods) reveals that the grain refinement dominates the yield strength enhancement, and its contribution was estimated to be 286 MPa. Owing to the ultralow elastic misfit (the lattice misfit is 0.11 %) and the disordered nature, the elastic and interfacial strengthening of the Cu-rich nanoprecipitates were estimated to be 19.9 and 0.08 MPa respectively (see Methods). Therefore, the main role of these coherent Cu-rich precipitates is to refine the grains, rather than to produce strong precipitation hardening which often causes the strength-ductility trade-off.

To uncover the role of Cu-rich nanoprecipitates in dislocation motion and nanotwin formation, we fabricate a UFG 0Cu alloy with a grain size of 1.1 ± 0.5 μm for comparison (see Methods and Extended Data Fig. 6a). In the early deformation stage (i.e., 15 % strain), a high density of dislocation walls and cells are observed in both alloys, along with some nanotwins with interspacing of 300–500 nm (Fig. 5a, b). The calculation of respective hardening contribution from nanotwins and dislocations demonstrates that dislocations dominate strain hardening for both steels during this stage, and the Cu-rich nanoprecipitates

exhibit a negligible effect on dislocation motion due to its small strengthening contribution (See Methods and Extended Data Fig. 6b).

A further increase of strain to 45 % leads to continuous formation of nanotwins in both UFG alloys (Fig. 5 c, d and Extended Data Fig. 7a, b). The average width and interspacing of the nanotwins in 4Cu are 7.9 ± 5.4 and 15.2 ± 14.3 nm, respectively, whilst those in UFG 0Cu are much larger, i.e., 15.6 ± 13.7 and 69.2 ± 38.4 nm, respectively. Due to the thinner and denser distribution of twins beyond 15 % strain, twinning gradually dominates the strain hardening in 4Cu, whereas dislocations still govern hardening in UFG 0Cu (Extended Data Fig. 6b)[34].

At the early stage of plastic deformation, part of the Cu-rich particles are sheared by dislocations and become elongated along the loading direction (Fig. 5e and Extended Data Fig. 7c), which is consistent with their weak strengthening effect. At the late stage, the Cu-rich precipitates are uniformly fragmented into smaller ones (Fig. 5f), leading to a much increased number density. The STEM EDS-SI images (Fig. 5g, h) confirm that the nanotwins frequently cut through the Cu-rich precipitates and in combination with dislocation shearing, caused the fragmentation, and in turn, the Cu-rich clusters refined nanotwins, leading to a twinning dominated stage of deformation. In contrast to full dislocation movement, twinning proceeds via co-operative motion of Shockley partials on the {111} planes. When the partial dislocations cut through the Cu-rich clusters, a stacking fault with higher energy in the Cu-rich clusters (78 mJ/m^2 for Cu[35] and 22 mJ/m^2 for matrix[36]) would emerge as an additional obstacle to resist subsequent twinning and constrain the growth of the twins, thus refining twinning substructures. More importantly, numerous small dislocation cells are observed around the thinner and denser nanotwins (Extended Data Fig. 7d, e), suggesting that the refined nanotwins could still accommodate additional dislocation accumulation, which is also critical for sustaining a continuous high strain hardening rate.

In summary, we have introduced a simple yet reliable approach to developing bulk UFG structures without introduction of any crystal defects. Such a grain-refinement strategy leads to development of the UFG structures that are not only highly stable, but also compatible with the typical deformation mechanisms of metallic materials, e.g., dislocation motion and multiplication, transformation induced plasticity and TWIP, thereby taking full advantage of fine grains and thereby substantially enhancing overall mechanical performance of UFG alloys. We summarized the alloy design principle and selection criterion of the strategic element (i.e., Cu in this study) in Methods, which could extend the current concept to other alloy systems (Extended Data Figs. 8) and facilitate exploration and development of advanced metallic materials.

Methods

Composition design.

To realize the rapid and copious nanoprecipitation, the selection of Cu in Fe-22Mn-0.6C was based on the following considerations: 1), Cu has a great tendency to precipitate out (i.e., the solubility of Cu in the matrix is very limited) but there is no chance to form intermetallic

compounds with the constituent elements, such as Fe, Mn and C; 2), the crystalline structure and lattice parameters of the austenitic matrix are almost identical with Cu, thus resulting in a very low lattice misfit $\left(\frac{a_{cu} - a_{matrix}}{a_{mtrix}} = 0.11\%\right)$ (a_{cu} = 0.3615 nm, for Fe-22Mn-0.6C austenite, a_{matrix} = 0.3611 nm), which significantly decreases the nucleation barrier for precipitation and also hampers the rapid coarsening of nanoprecipitates; 3), Cu-rich precipitates are a fully coherent disordered nanophase, and thus exhibit weak resistance on dislocation motion and refine nanotwins, leading to a superb combination of strength and ductility.

Specimen preparation.

Alloy ingots with compositions of Fe-22Mn-0.6C-xCu (x= 0, 3, 4, 5, wt %) were prepared by arc-melting. The ingots were re-melted at least 5 times under argon atmosphere and then were cast into a $45 \times 12 \times 70$ mm^3 copper mould. The as-cast ingots were cold rolled to a thickness of 6 mm firstly and then homogenized at 1040°C for 3 h under Ar atmosphere. The results show that for 5Cu, Cu cannot be fully dissolved into the matrix after solid solution treatment and localized melting would occur, so, in this work, we focused on the study of 0Cu, 3Cu, and 4Cu. The homogenized materials were cold rolled again from 6 to 1.5 mm and subsequently annealed at 760, 810, 860 and 910 °C for 5 min respectively, followed by water quenching. The 1.5 mm sheets of 0Cu and 4Cu were also annealed at 760°C for 20, 40 and 60 min. To achieve an ultrafine structure, the 0Cu was cold rolled from 8 to 4 mm and annealed at 800°C for 5 min to refine the coarse grains after homogenization. Then the 4 mm thick plate was cold rolled again to 1.5 mm and flash annealed at 760 °C for 2 min. The chemical compositions of 0Cu, 3Cu and 4Cu after annealing were analysed using ICP-OES instrument for Fe, Mn and Cu elements and Leco ONH836 instrument for C and the results are listed in Extended Data Table 1. Sheet tensile samples with a gauge length of 15 mm and cross-section of 1.5×3 mm^2 were cut and mechanically polished to 2000 grit size. Tensile tests were performed on a Zwick/Roell Z050 with laser extensometer at a strain rate of 4×10^{-4} s^{-1} at room temperature. Tensile force was applied in the rolling direction. At least 5 samples were tested for each condition.

Microstructure characterization.

Samples for EBSD imaging were mechanically polished down to 3 μm diamond suspension. Prior to EBSD observation, the samples were polished using a Gatan PECS™ II at 5 kV, 5° for 0.5 h. EBSD was performed using a field emission gun scanning electron microscope (FEI Inspect F50) operating at 20 kV with a step size in the range of 0.05 to 0.2 μm, depending on the sample grain size. EBSD data was analysed using HKL's CHANNEL5 software to determine the average grain size and at least 1000 grains were used. The X-ray diffraction measurement was conducted for as-rolled 4Cu, and 4Cu and UFG 0Cu with 15 % and 45 % strain to calculate the dislocation density using Bruker D2 Phaser with a scan increment size of 0.02°. To obtain the melting point of 4Cu, the homogenized 4Cu was used to conduct differential thermal analysis using a Simultaneous Thermal Analyser, Netzsch TG 449 F3 Jupiter. 0.25 g material was heated from 20 to 1450 °C under a flowing argon atmosphere at a heating rate of 10 °C/minute. Thin foil samples for TEM and STEM analysis were prepared by twin-jet electropolishing with a solution of 5 % perchloric acid,

35 % 2-butoryethanol and 60 % methanol at −35 °C. A FEI Titan 80–300 STEM/TEM equipped with a monochromator and a probe spherical-aberration corrector and a JEOL-F200 were employed to perform electron diffraction, diffraction-contrast imaging, STEM imaging and STEM-EDS imaging. Atomic-resolution ADF-STEM images were acquired with an operating voltage of 300 kV, a probe semi-convergence angle of 24 mrad and a HAADF detector collection angle of 57–325 mrad. The APT characterizations were performed in a CAMECA Instruments LEAP 5000XR. Specimens for APT were prepared in a scanning electron microscope/focused-ion beam. The data was acquired in voltage mode, with a specimen temperature of 50 K, a pulse repetition rate of 200 kHz, a pulse fraction of 15 % and an ion collection rate of 0.5 % per field evaporation pulse. The APT data was reconstructed using Cameca IVAS 3.8.4 and the reconstruction was calibrated based on elements of crystallography retained within the data characterized by spatial distribution maps[37,38]. To obtain a misorientation map with high resolution, a NanoMEGAS DigiSTAR™ system was employed to analyse the 4Cu with 45 % strain using a 1.5 nm step size, and the results were analysed using HKL's CHANNEL5 software. Phase analysis of the recrystallized 4Cu was investigated by a synchrotron-based high-energy X-ray diffraction technique at the 11-ID-C beam line of the Advanced Photon Source, Argonne National Laboratory, USA. A monochromatic X-ray beam with wavelength 0.01173 nm was used. The equilibrium Cu solubility in the austenite with a composition of Fe-22Mn-0.6C (wt %) was calculated using JMatPro over a temperate range of 650 to 950 °C.

Correction of particle compositions.

Owing to the effect of trajectory aberrations on the composition of small particles, we corrected the compositions using the methods proposed by Blavette et al[39]. We selected three sets of particles with diameter in the range of 2.5–3, 4.5–5 and 6–7 nm to reveal the effect of trajectory aberrations. The composition profiles of these Cu-rich precipitates are shown in Extended Data Fig. 5a. As expected, the relative density (ρ_r) across the particles is higher than that of the matrix, and the smaller particles have higher ρ_r. Nevertheless, the value of ρ_r is consistently lower than 1.6 (Extended Data Fig. 5a). As proposed by Blavette et al.[39], the corrected composition is given by $C\beta' = C\beta + (C\beta - C\alpha) * \eta$, where the correction factor η is dependent on the change of the relative local atomic density (Extended Data Fig. 5b). As can be seen in Extended Data Fig. 5b, when the value of ρ_r is lower than 1.6, the particle composition is just slightly affected by trajectory aberrations because η is close to zero. After the correction, the corrected Cu contents of these three sets of particles are 59 ± 2 at %, 73 ± 3 at % and 80 ± 2 at % (Extended Data Fig. 5c), respectively, confirming that Cu content increases with particle growth.

Calculation of dislocation density.

Modified Williamson–Hall plots were used to calculate the dislocation density from the XRD profiles of as-rolled 4Cu, and the 4Cu and UFG 0Cu pre-tensioned to 15 % and 45 % strain for the calculation of driving pressure for recrystallization and the individual strengthening effect of different strengthening mechanisms. The diffraction profiles used for this analysis were the (1 1 1), (2 0 0), (2 2 0), (3 1 1), (2 2 2) reflections of the austenite phase.

According to the modified Williamson–Hall methods, the average crystalline size, dislocation density and planar defects (stacking fault and twinning) all contribute to the broadening of diffraction peaks, as illustrated in the following modified Williamson–Hall equation[40]:

$$\Delta K - \beta W_{hkl} = \frac{0.9}{D} + \left(\frac{\pi A^2 b^2}{2}\right)^{\frac{1}{2}} \rho^{\frac{1}{2}} K \overline{C}^{\frac{1}{2}} + O\left(K^4 \overline{C}^2\right)$$

While $K = 2\sin\theta/\lambda$ and $\Delta K = 2\cos\theta(\Delta\theta)/\lambda$. Here, $\Delta\theta$, θ, and λ represent the full widths at half-maxim (FWHM) of diffraction peaks at θ_B, diffraction angle, and wavelength of the X-rays, respectively. In the current research, the Cu radiation with value of $\lambda = 0.15405$ nm was applied. D, ρ, and b represent average grain size, dislocation density, and the magnitude of the Burgers vector, respectively. A is a constant depending on both the effective outer cut-off radius of dislocations and the dislocation density. β is a constant related to the effect of twinning and stacking fault which can be calculated by trial-and-error through curve fitting of $\Delta K - \beta W_{hkl}$-$K\overline{C}^{1/2}$ plot. h, k and l are the Miller's indices and W_{hkl} is coefficient related to hkl lattice plane. O is the higher order term of $K\overline{C}^{1/2}$. The dislocation contrast factor $\overline{C}$ can be expressed as[41]:

$$\overline{C} = \overline{C}_{hoo}\left\{1 - q\left[\frac{h^2k^2 + k^2l^2 + l^2h^2}{\left(h^2 + k^2 + l^2\right)^2}\right]\right\}$$

Where $\overline{C}_{h00}$ and q are constants and can be obtained from anisotropic elastic constants of materials[41]. The austenite peaks including (1 1 1), (2 0 0), (2 2 0), (3 1 1), (2 2 2) reflections are listed in the ($\Delta K - \beta W_{hkl}$) vs $K\overline{C}^{1/2}$ plot (Extended Data Fig. 9). The values of dislocation density ρ and average crystal size D can be further determined from the best linear fitting between $\Delta K - \beta W_{hkl}$ and $K\overline{C}^{1/2}$ (Extended Data Fig. 9).

Calculations of P_z, P_r and P_g[42]

$$P_z = \frac{3F_v\gamma}{2r}$$

$$P_r = \alpha\rho Gb^2$$

$$P_g = \frac{2\gamma}{R}$$

where r and R are the mean radii of precipitates and recrystallized grains, γ is the high grain boundary energy of ~ 0.6 J/m^2 for austenite steel[43], F_v is local volume fraction of

nanoprecipitates and can be expressed as: $F_v = \frac{4\pi r^3 N_v}{3}$ N_v is the number density of nanoprecipitates in one unit volume, α is a constant of ~ 0.5, the typical average dislocation density ρ was calculated from XRD profiles, G and b are the shear modulus and Burgers vector and for Fe-22Mn-0.6C steel are 65 GPa and 0.25 nm, respectively[44]. The averaged grain size, precipitates' size and volume fraction of precipitates are obtained from STEM images, EBSD results and APT results.

Precipitation hardening.

For coherency strengthening, the stress increment can be described by[45]:

$$\Delta\sigma_{coherency} = 4.1 M G \varepsilon^{3/2} (fr/b)^{1/2}$$

where M is the Taylor factor of 3, G is the shear modulus of 65 GPa, ε is the lattice misfit of 0.11 %, f is the nanoprecipitate volume fraction of 4.2 %, r is the radius of Cu-rich nanoprecipitates (2.8 nm) and b is Burgers vector of 0.25 nm. $\sigma_{coherency}$ was then calculated to be 19.9 MPa.

For chemical strengthening, the stress increment can be described by[46]:

$$\Delta\sigma_{chemical} = \left(\frac{6\gamma_s^3 bf}{\pi T r^2}\right)^{1/2}$$

Where γ_s is the specific interface energy of 0.017 J/m^2 [45], T is the line tension of the dislocations, approximately equal to $Gb^2/2$[45]. $\sigma_{chemical}$ was calculated to be 0.08 MPa.

Therefore, the total strengthening contribution of precipitation is around 20 MPa.

Grain refinement hardening.

The effect of grain size on yield stress (σ_{ys}) can be expressed as: $\sigma_{ys} = \sigma_0 + \frac{k_y}{\sqrt{d}}$ Where σ_0 is the lattice friction stress, k_y is the strengthening coefficient and d is the grain size. To calculate the yield strength of 4Cu with a grain size of 800 nm, the values of σ_0 and k_y were adopted from that of the matrix, i.e., the 22Mn-0.6C steel, where σ_0 is $\approx$ 170 MPa and k_y is 428 MPa $\mu m^{\frac{1}{2}}$, thus for the 4Cu alloy with a grain size of 800 nm, σ_{ys} is determined to be 651 MPa. As for 0Cu annealed at 760°C for 5 min, the yield stress is 365 MPa, the stress increment due to grain refinement is 286 MPa.

Thus, the total strength increment due to grain refinement and precipitation hardening amounts to 306 MPa, which agrees with the experimental result of 345 MPa that also includes the contributions of Cu solid solution strengthening.

Twinning and dislocation hardening.

We further calculated the individual strengthening contribution of dislocation and twinning in 4Cu and UFG 0Cu pre-tensioned to 15 % and 45 % strain. By using the modified Williamson–Hall plots of the XRD patterns (Extended Data Fig. 9), the dislocation densities (ρ) of 4Cu and UFG 0Cu for the 15 % strain are 3.5×10^{15} and 3.9×10^{15} m^{-2} respectively, but change to 6.4×10^{15} and 1.6×10^{16} m^{-2}, respectively, for the 45 % strain. The flow strength after yielding can be expressed as:

$$\sigma_{\text{fellow}} = \sigma_0 + \frac{k_y}{\sqrt{d}} + \sigma_d + \sigma_t$$

Where σ_d is the contribution of dislocation hardening and σ_t is the contribution of twinning hardening. σ_d can be calculated using the Taylor hardening low: $\sigma_d = M\alpha\mu b\sqrt{\rho}$, where M is the Taylor factor, which is 3.06 for austenitic steel[44], α is a geometrical factor with a value of 0.136 for TWIP steels[34], μ is the shear modulus and taken to be 65 GPa for the current base alloy[44], b is the magnitude of the Burgers vector, which is 0.25 nm[44]. For 4Cu and UFG 0Cu alloys at the strain of 15%, σ_d was thus calculated to be 396 and 418 MPa, respectively, then increased to 536 and 867 MPa, respectively, at the strain of 45 %. σ_t was estimated to be 34 and 714 MPa for 4Cu at the strain of 15% and 45%, respectively, whilst 46 and 368 MPa for UFG 0Cu, respectively. The results are summarized in Extended Data Fig. 6b.
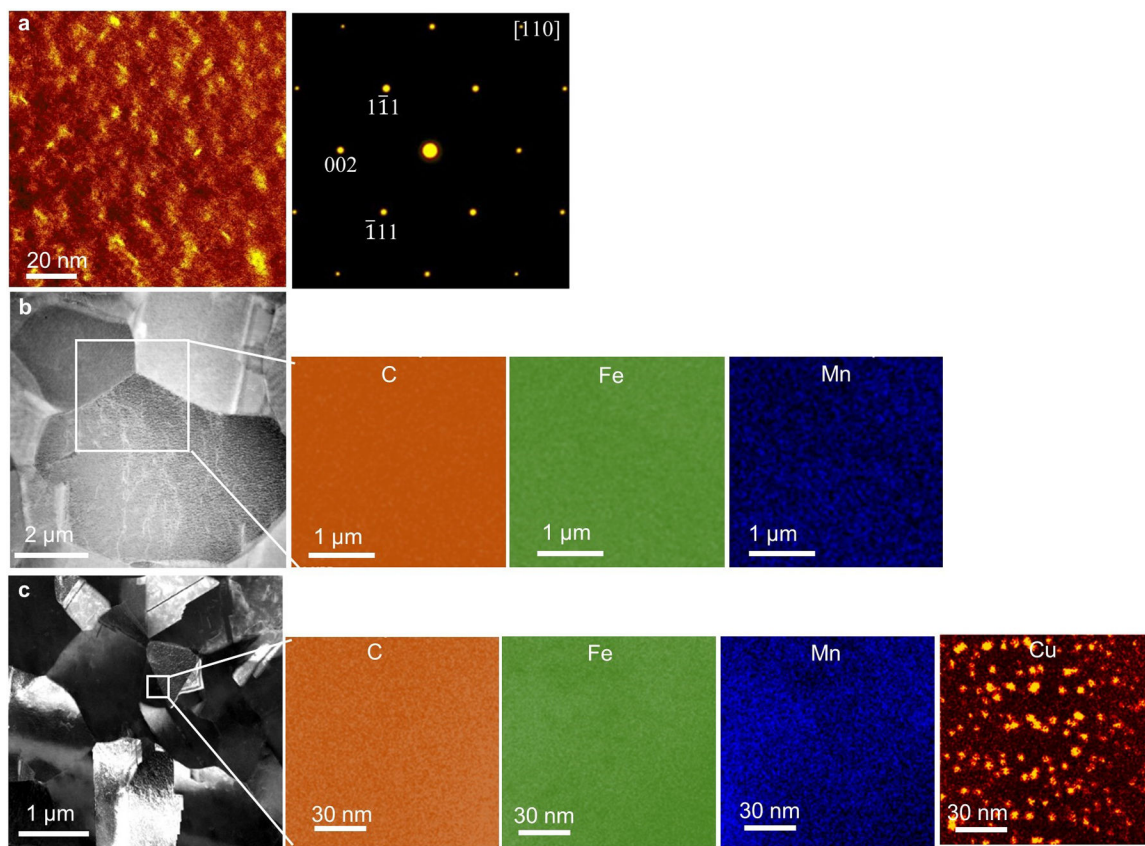
Extended Data
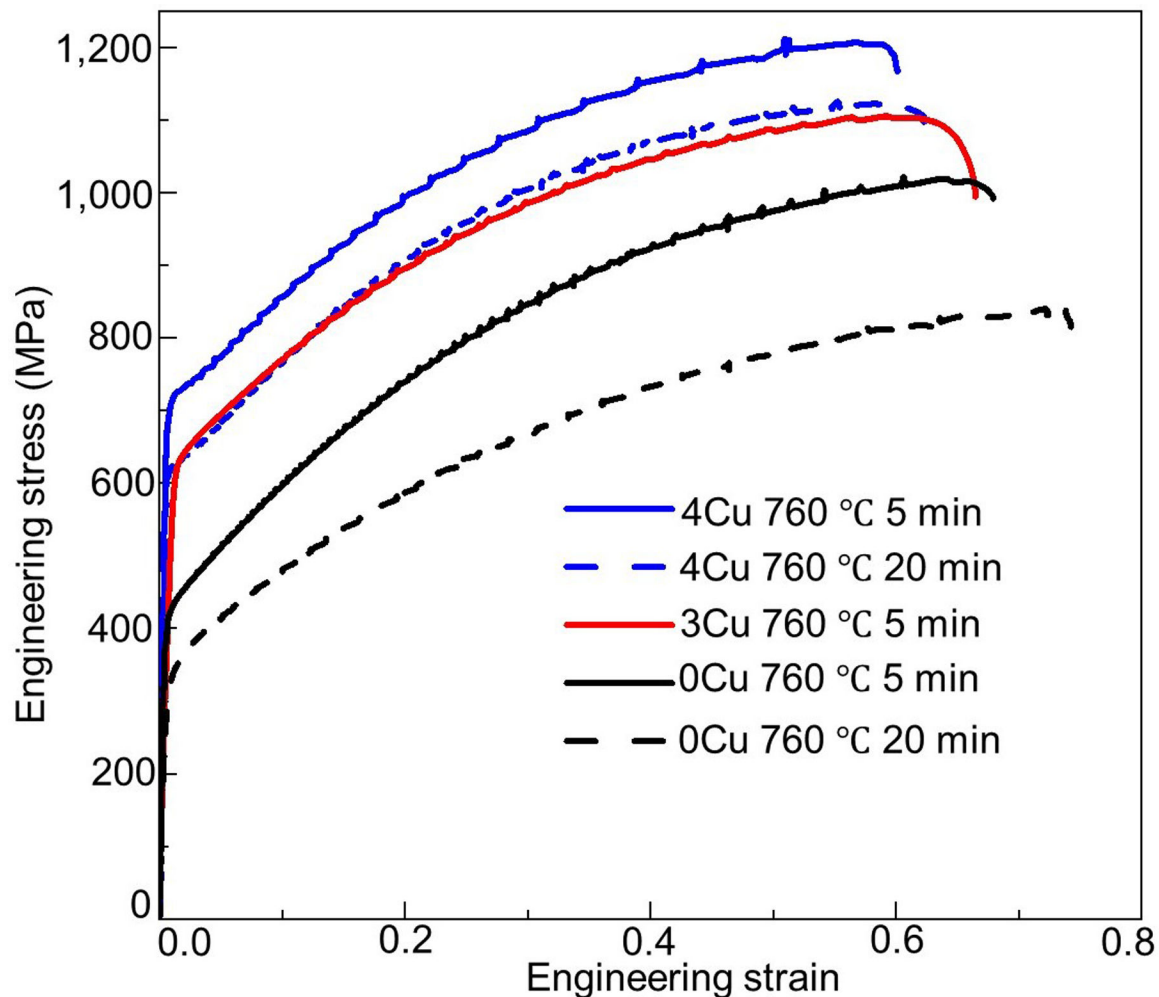
**Extended Data Figure 1. Mechanical properties.**
Engineering stress-strain curves of 0Cu, 3Cu and 4Cu annealed at 760 °C for 5 and 20 min.
With additions of Cu, both the yield strength and ultimate tensile strength increased
remarkably with comparable ductility of 0Cu.

**Extended Data Figure 2. ADF-STEM analysis of the 4Cu, 0Cu and 3Cu annealed at 760°C for 5 min.**
a, ADF image of 4Cu showing a high density of nanoprecipiates and the corresponding SAED pattern showing only the matrix reflection of the $[110]_{fcc}$ zone axis without any extra reflection of the precipitates. **b**, ADF image of 0Cu showing an average grain size of 2.2 μm. **c**, ADF image of 3Cu presenting a UFG structure with a high density of nanoprecipitates. No elemental segregation at grain boundaries was detected.
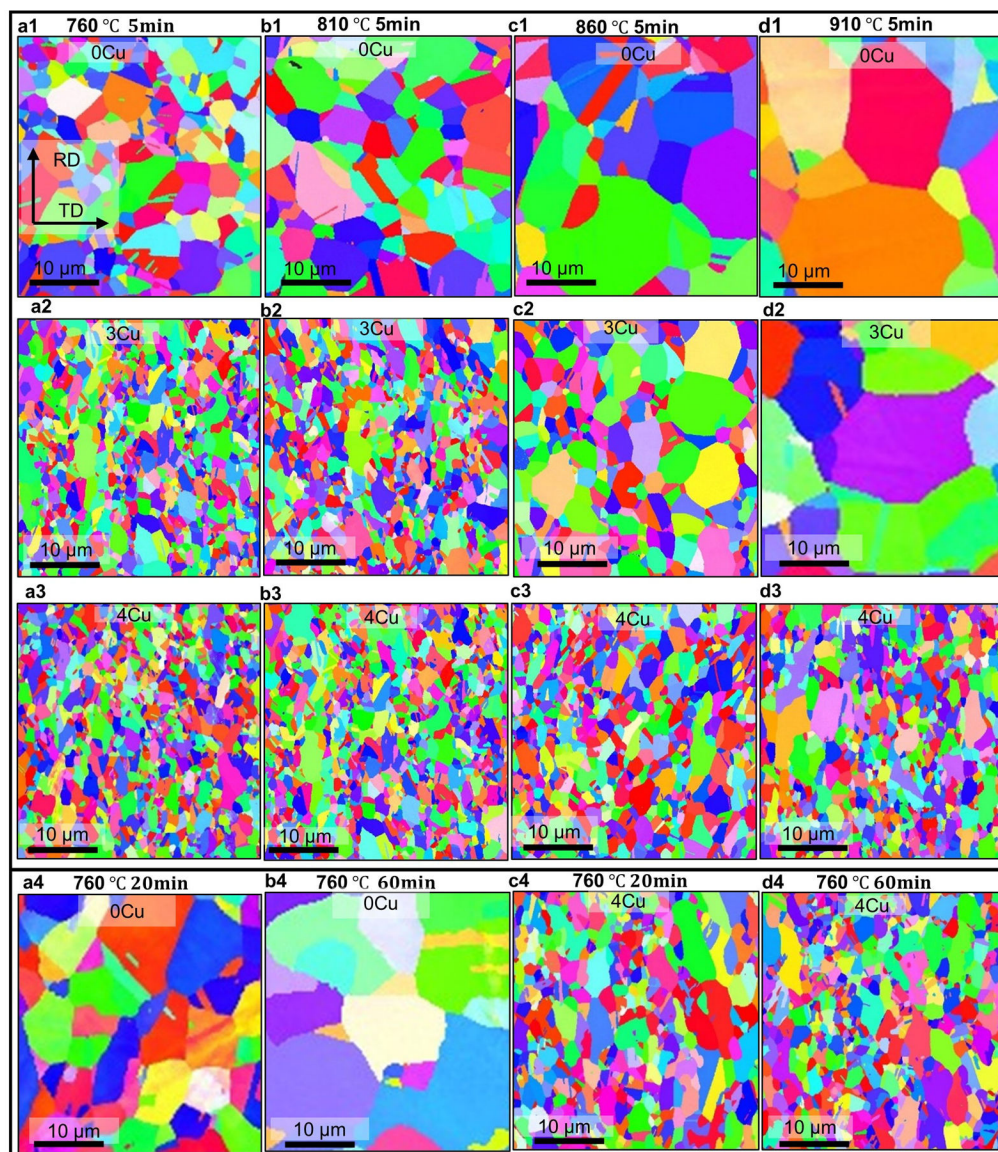
Extended Figure 3. Thermal stability evaluation of UGF structures.
EBSD analysis of 0Cu (**a1**-**d1**), 3Cu (**a2**-**d2**) and 4Cu (**a3**-**d3**) annealed at 760, 810, 860 and 910 °C for 5 min, respectively. **a4**, **b4**, EBSD maps of 0Cu annealed at 760 °C for 20 and 60 min, respectively. **c4**, **d4**, EBSD maps of 4Cu annealed at 760 °C for 20 and 60 min, respectively. Owing to the enhanced thermal stability, UFG structures of the Cu-doped alloys can be obtained in a wide range of annealing temperature and time.
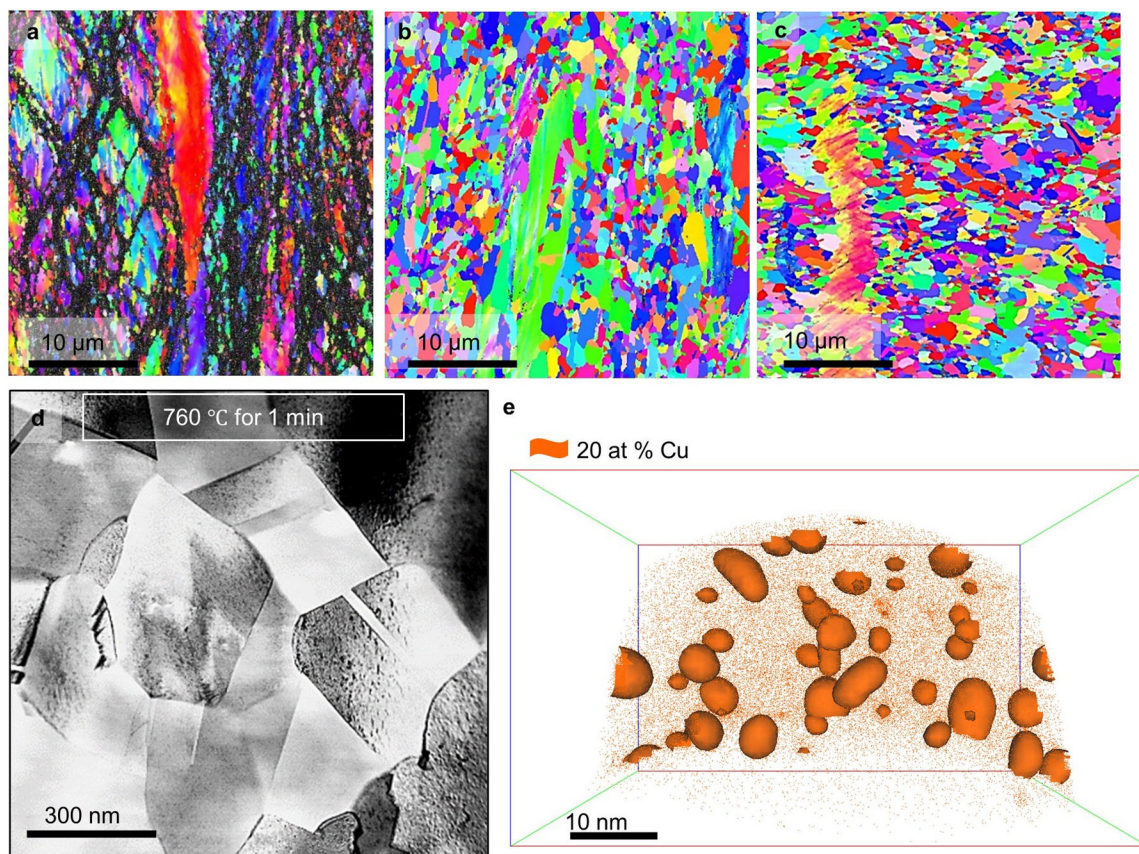
Extended Data Figure 4. Microstructural analysis of 4Cu annealed at 760°C for 0.5, 1 and 2 min.
a-c, EBSD analysis of 4Cu annealed at 760 °C for 0.5, 1, and 2 min, restively, revealing that nucleation for recrystallization occurred extensively after 0.5 min annealing. As the annealing time extends from 1 to 2 min, the volume fraction of the recrystallized matrix increases from 76 to 95 %. **d, e**, ABF-STEM image and the reconstruction of APT dataset of 1 min annealed 4Cu presenting the formation of equiaxed grains of 300 ± 150 nm and Cu-rich precipitates with an average size of 3.7 nm and a number density of 8.8×10^{23} m^{-3}. The isoconcentration surfaces are 20 at % Cu.

a 30 at % Cu

b

$$\eta = 0.0808\rho_r{}^3 - 0.3953\,\rho_r{}^2 + 0.6996\rho_r - 0.4176$$

c
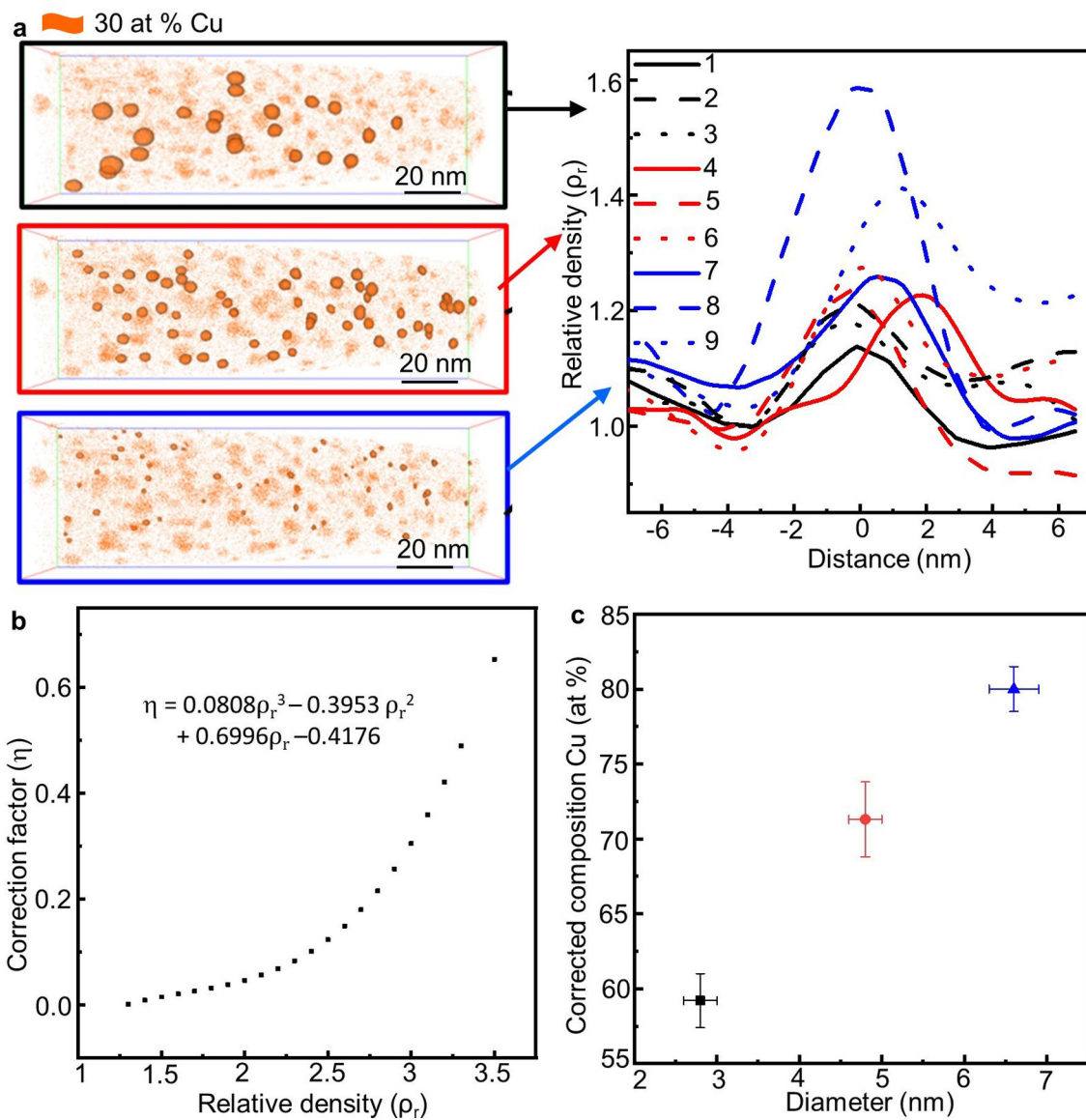
Extended Data Figure 5. Effect of the trajectory aberrations of APT on the composition analysis of particles.

The error bars are standard deviations of the mean. The isoconcentration surfaces are 30 at % Cu.
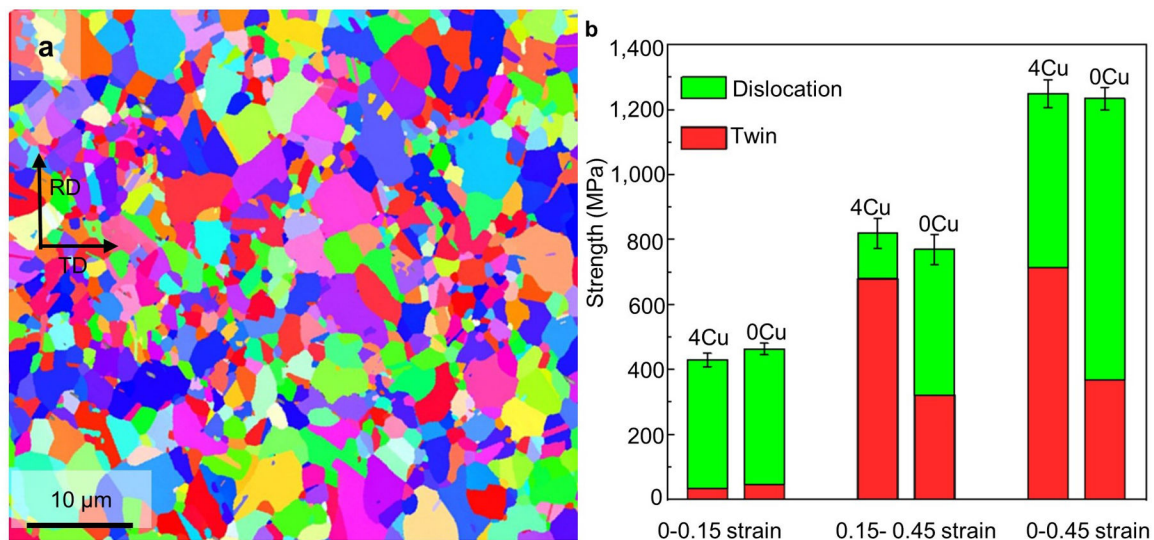
Extended Data Figure 6. EBSD map of UFG 0Cu and calculation of individual strengthening contribution of dislocations and nanotwins of UFG 0Cu and 4Cu.
a, EBSD map of UFG 0Cu processed by a two-step cold rolling and flash annealing process presents a grain size of 1.1 ± 0.5 μm. **b**, Twinning gradually dominates the strengthening beyond 15 % strain in 4Cu, whilst dislocation multiplication governs the strengthening in the entire deformation stage of the UFG 0Cu.
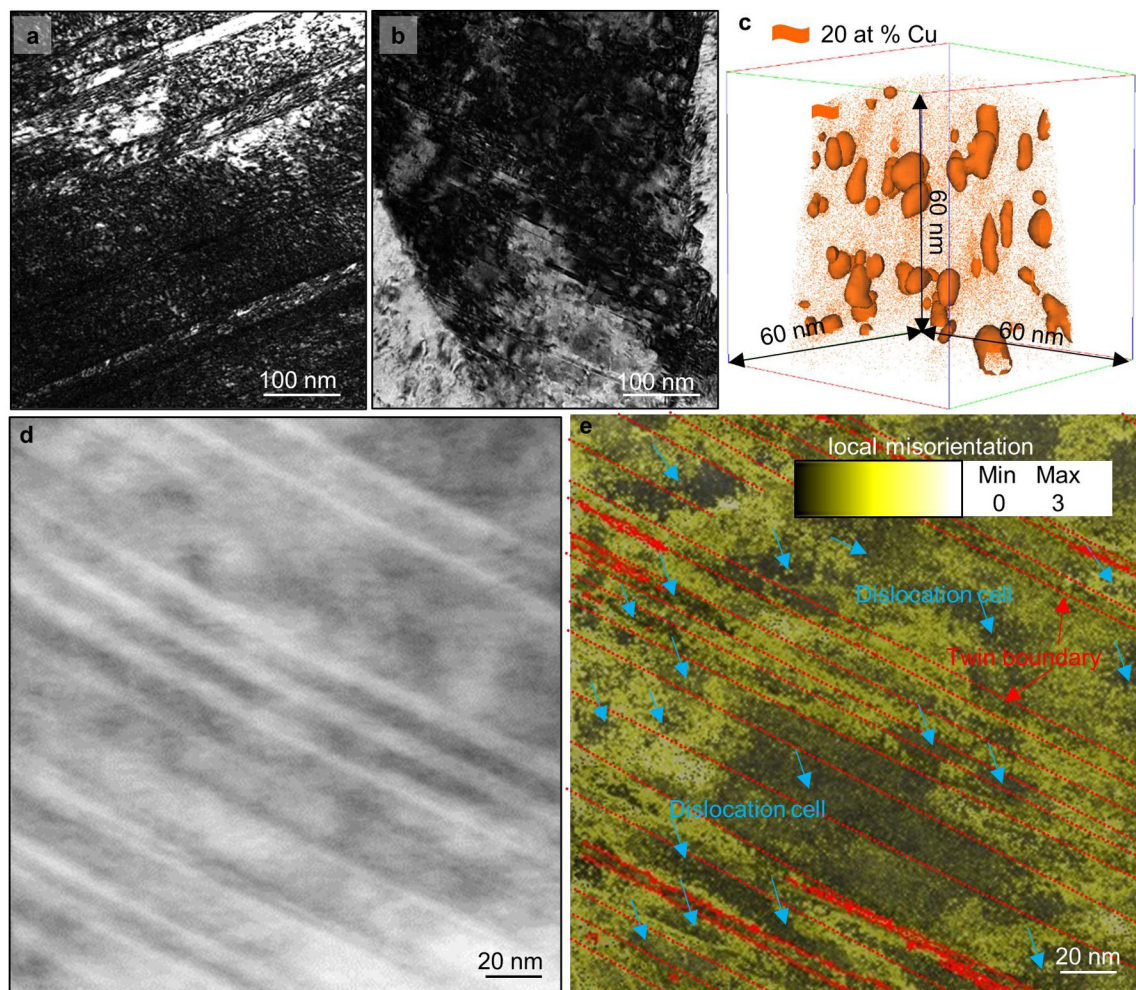
Extended Data Figure 7. Deformed microstructure analysis of 4Cu pre-strained to 15 and 45 %. **a, b,** The corresponding bright-field images of Fig. 5c and d, respectively, showing a high density of dislocations and nanotwins with interspacing of 300–500 nm. **c,** Reconstructed APT data of 4Cu prestrained to 15 % presenting some of nanoprecipitates flattened along the loading direction. **d, e,** Bright-field TEM image and its corresponding high-resolution misorientation map superimposed with nanotwin boundaries (solid red lines: indexed nanotwin boundaries; thin dashed red lines: nonindexed nanotwin boundaries) obtained using a NanoMEGAS DigiSTAR™ system with a step size of 1.5 nm. Numerous small dislocation cells (blue arrows) were observed in nanotwins and their interspaces. The isoconcentration surfaces are 20 at % Cu.
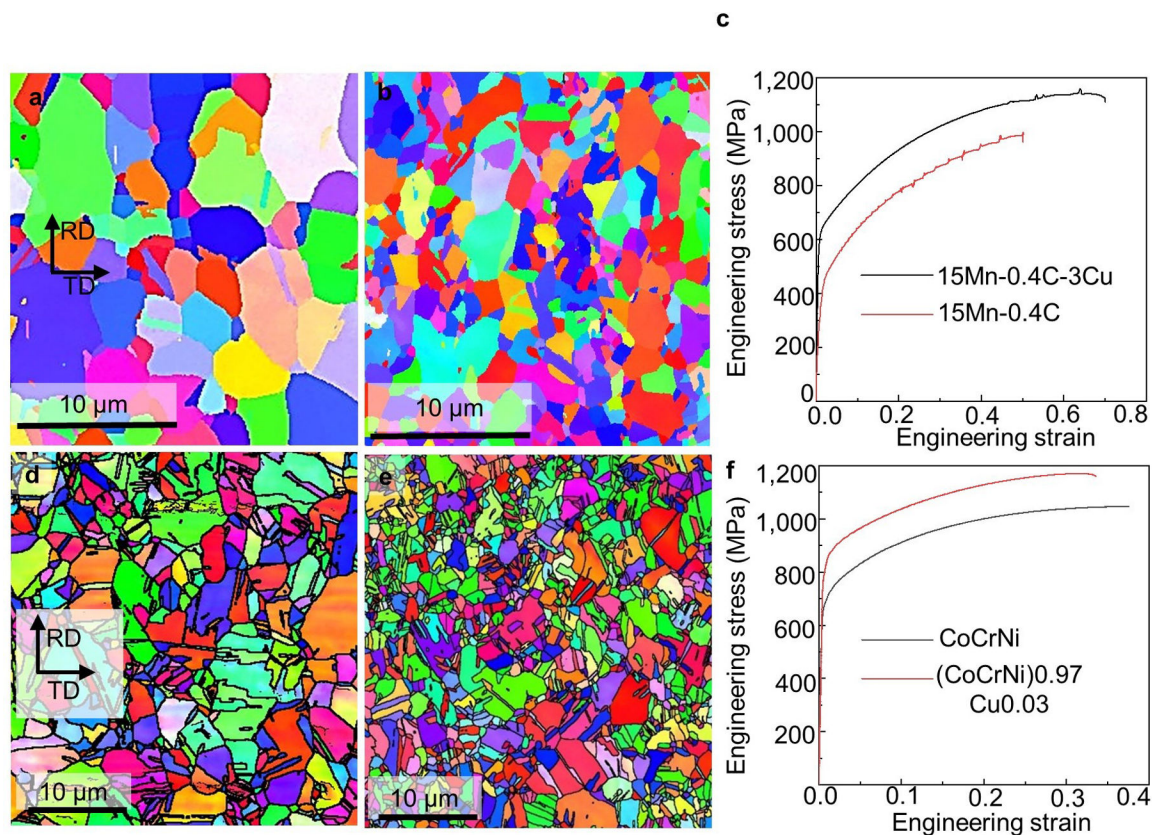
Extended Data Figure 8. Microstructure and mechanical property analyses of TRIP steels and medium entropy alloys with minor Cu addition.

a-c, EBSD maps and tensile stress-strain curves of the TRIP steels with a composition of Fe-15Mn-0.4C and Fe-15Mn-0.4C-3Cu (wt %), respectively, after annealing at 730 °C for 5 min. **d-f,** EBSD maps and tensile stress-strain curves of 33Co33Cr34Ni and (33Co33Cr34Ni)0.97Cu0.03 (at. %) after annealing at 810 °C for 10 min. The alloys with minor Cu addition exhibit finer microstructures and enhanced mechanical properties.
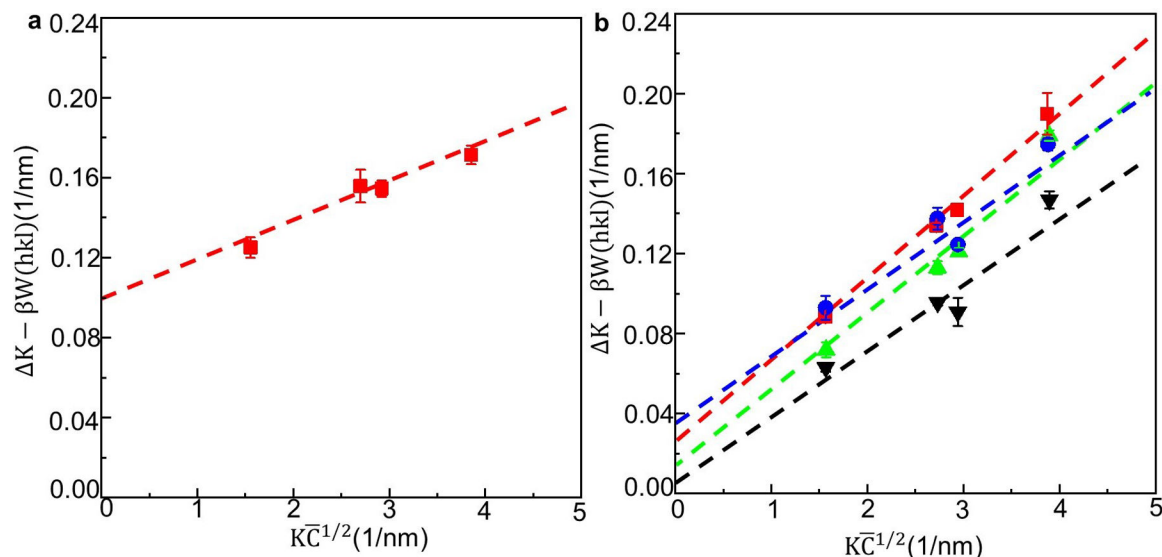
Extended Data Figure 9. Modified Williamson-Hall plots of FWHM (full width at the half maximum) as a function of $K\overline{C}^{1/2}$.
a, Peak broadening analysis on cold rolled 4Cu alloys. **b**, Peak broadening analysis on the prestrained UFG 0Cu and 4Cu alloys.

Extended Data Table 1.

Composition (wt %) of 0Cu, 3Cu and 4Cu alloys according to chemical analysis using ICP-OES instrument for Fe, Mn and Cu and Leco ONH836 instrument for C.

Alloy/Element	Mn (wt %)	C (wt %)	Cu (wt %)	Fe (wt %)
0Cu	21.74	0.58	--	Bal.
3Cu	21.93	0.55	2.67	Bal.
4Cu	21.61	0.59	3.84	Bal.

Acknowledgements

## References

1. Howe A Ultrafine grained steels: industrial prospects. Materials Science and Technology 16, 1264–1266 (2000).

2. Song R, Ponge D, Raabe D, Speer JG & Matlock DK Overview of processing, microstructure and mechanical properties of ultrafine grained bcc steels. Materials Science and Engineering: A 441, 1–17, doi:10.1016/j.msea.2006.08.095 (2006).

3. Funakawa Y, Shiozaki T, Tomita K, Yamamoto T & Maeda E Development of high strength hot-rolled sheet steel consisting of ferrite and nanometer-sized carbides. ISIJ international 44, 1945–1951 (2004).

4. Song R, Ponge D & Raabe D Mechanical properties of an ultrafine grained C–Mn steel processed by warm deformation and annealing. Acta Materialia 53, 4881–4892, doi:10.1016/j.actamat.2005.07.009 (2005).

5. Ohmori A, Torizuka S & Nagai K Strain-hardening due to dispersed cementite for low carbon ultrafine-grained steels. ISIJ international 44, 1063–1071 (2004).

6. Chen Z, Bong HJ, Li D & Wagoner R The elastic–plastic transition of metals. International Journal of Plasticity 83, 178–201 (2016).

7. Bouaziz O, Zurob H & Huang M Driving Force and Logic of Development of Advanced High Strength Steels for Automotive Applications. steel research international 84, 937–947, doi:10.1002/srin.201200288 (2013).

8. Grässel O, Krüger L, Frommeyer G & Meyer LW High strength Fe–Mn–(Al, Si) TRIP/TWIP steels development — properties — application. International Journal of Plasticity 16, 1391–1409, doi:10.1016/S0749-6419(00)00015-2 (2000).

9. Zhao J. l., Xi Y, Shi W & Li L Microstructure and Mechanical Properties of High Manganese TRIP Steel. Journal of Iron and Steel Research, International 19, 57–62, doi:10.1016/S1006-706X(12)60088-0 (2012).

10. Zhang M, Li L, Fu RY, Krizan D & De Cooman BC Continuous cooling transformation diagrams and properties of micro-alloyed TRIP steels. Materials Science and Engineering: A 438–440, 296–299, doi:10.1016/j.msea.2006.01.128 (2006).

11. Gu X, Xu Y, Peng F, Misra RDK & Wang Y Role of martensite/austenite constituents in novel ultra-high strength TRIP-assisted steels subjected to non-isothermal annealing. Materials Science and Engineering: A 754, 318–329, doi:10.1016/j.msea.2019.03.070 (2019).

12. Huang JN et al. Combining a novel cyclic pre-quenching and two-stage heat treatment in a low-alloyed TRIP-aided steel to significantly enhance mechanical properties through microstructural refinement. Materials Science and Engineering: A 764, 138231, doi:10.1016/j.msea.2019.138231 (2019).

13. De Moor E, Speer JG, Matlock DK, Kwak J-H & Lee S-B Effect of carbon and manganese on the quenching and partitioning response of CMnSi steels. ISIJ international 51, 137–144 (2011).

14. Gwon H, Kim J-K, Shin S, Cho L & De Cooman BC The effect of vanadium micro-alloying on the microstructure and the tensile behavior of TWIP steel. Materials Science and Engineering: A 696, 416–428, doi:10.1016/j.msea.2017.04.083 (2017).

15. Tian Y et al. A novel ultrafine-grained Fe22Mn0. 6C TWIP steel with superior strength and ductility. Materials Characterization 126, 74–80 (2017).

16. Dini G, Najafizadeh A, Ueji R & Monir-Vaghefi SM Improved tensile properties of partially recrystallized submicron grained TWIP steel. Materials Letters 64, 15–18, doi:10.1016/j.matlet.2009.09.057 (2010).

17. Kim YW, Kim JH, Hong S-G & Lee CS Effects of rolling temperature on the microstructure and mechanical properties of Ti–Mo microalloyed hot-rolled high strength steel. Materials Science and Engineering: A 605, 244–252 (2014).

18. Arlazarov A, Bouaziz O, Hazotte A, Gouné M & Allain S Characterization and modeling of manganese effect on strength and strain hardening of martensitic carbon steels. ISIJ international 53, 1076–1080 (2013).

19. Kim S-H, Kim H & Kim NJ Brittle intermetallic compound makes ultrastrong low-density steel with large ductility. Nature 518, 77, doi:10.1038/nature14144 (2015). [PubMed: 25652998]

20. Chan HL, Ruan HH, Chen AY & Lu J Optimization of the strain rate to achieve exceptional mechanical properties of 304 stainless steel using high speed ultrasonic surface mechanical attrition treatment. Acta Materialia 58, 5086–5096, doi:10.1016/j.actamat.2010.05.044 (2010).

21. Zhou P, Liang Z, Liu R & Huang M Evolution of dislocations and twins in a strong and ductile nanotwinned steel. Acta Materialia 111, 96–107 (2016).

22. Sohn SS et al. Ultrastrong Medium-Entropy Single-Phase Alloys Designed via Severe Lattice Distortion. Advanced Materials 31, 1807142 (2019).

23. Rahman KM, Vorontsov VA & Dye D The effect of grain size on the twin initiation stress in a TWIP steel. Acta Materialia 89, 247–257, doi:10.1016/j.actamat.2015.02.008 (2015).

24. Jiang S et al. Ultrastrong steel via minimal lattice misfit and high-density nanoprecipitation. Nature 544, 460, doi:10.1038/nature22032 (2017). [PubMed: 28397822]

25. Blavette D, Cadel E, Fraczkiewicz A & Menand A Three-dimensional atomic-scale imaging of impurity segregation to line defects. Science 286, 2317–2319 (1999). [PubMed: 10600736]

26. Chookajorn T, Murdoch HA & Schuh CA Design of stable nanocrystalline alloys. Science 337, 951–954 (2012). [PubMed: 22923577]

27. Park K-T, Kim Y-S, Lee JG & Shin DH Thermal stability and mechanical properties of ultrafine grained low carbon steel. Materials Science and Engineering: A 293, 165–172, doi:10.1016/S0921-5093(00)01220-X (2000).

28. Stráská J, Jane ek M, ížek J, Stráský J & Hadzima B Microstructure stability of ultrafine grained magnesium alloy AZ31 processed by extrusion and equal-channel angular pressing (EX–ECAP). Materials Characterization 94, 69–79, doi:10.1016/j.matchar.2014.05.013 (2014).

29. Hasegawa H et al. Thermal stability of ultrafine-grained aluminum in the presence of Mg and Zr additions. Materials Science and Engineering: A 265, 188–196, doi:10.1016/S0921-5093(98)01136-8 (1999).

30. Fan D & Chen L-Q Diffusion-controlled grain growth in two-phase solids. Acta materialia 45, 3297–3310 (1997).

31. Haase C et al. On the deformation behavior of κ-carbide-free and κ-carbide-containing high-Mn light-weight steel. Acta Materialia 122, 332–343, doi:10.1016/j.actamat.2016.10.006 (2017).

32. Yao MJ et al. Strengthening and strain hardening mechanisms in a precipitation-hardened high-Mn lightweight steel. Acta Materialia 140, 258–273, doi:10.1016/j.actamat.2017.08.049 (2017).

33. Takeuchi A & Inoue A Classification of bulk metallic glasses by atomic size difference, heat of mixing and period of constituent elements and its application to characterization of the main alloying element. Materials Transactions 46, 2817–2829 (2005).

34. Liang ZY, Li YZ & Huang MX The respective hardening contributions of dislocations and twins to the flow stress of a twinning-induced plasticity steel. Scripta Materialia 112, 28–31, doi:10.1016/j.scriptamat.2015.09.003 (2016).

35. Murr LE Interfacial phenomena in metals and alloys. (1975).

36. De Cooman BC, Estrin Y & Kim SK Twinning-induced plasticity (TWIP) steels. Acta Materialia 142, 283–362, doi:10.1016/j.actamat.2017.06.046 (2018).

37. Gault B et al. Advances in the calibration of atom probe tomographic reconstruction. Journal of Applied Physics 105, 034913 (2009).

38. Moody MP, Gault B, Stephenson LT, Haley D & Ringer SP Qualification of the tomographic reconstruction in atom probe by advanced spatial distribution map techniques. Ultramicroscopy 109, 815–824 (2009). [PubMed: 19362421]

39. Blavette D, Duval P, Letellier L & Guttmann M Atomic-scale APFIM and TEM investigation of grain boundary microchemistry in Astroloy nickel base superalloys. Acta Materialia 44, 4995–5005 (1996).

40. Ungár T, Ott S, Sanders PG, Borbély A & Weertman JR Dislocations, grain size and planar faults in nanostructured copper determined by high resolution X-ray diffraction and a new procedure of peak profile analysis. Acta Materialia 46, 3693–3699, doi:10.1016/S1359-6454(98)00001-9 (1998).

41. Ungár T, Dragomir I, Révész Á & Borbély A The contrast factors of dislocations in cubic crystals: the dislocation model of strain anisotropy in practice. Journal of applied crystallography 32, 992–1002 (1999).

42. Humphreys FJ & Hatherly M Recrystallization and related annealing phenomena. (Elsevier, 2012).

43. Caul M, Fiedler J & Randle V Grain-boundary plane crystallography and energy in austenitic steel. Scripta Materialia 35, 831–836, doi:10.1016/1359-6462(96)00234-5 (1996).

44. Bouaziz O, Allain S & Scott C Effect of grain and twin boundaries on the hardening mechanisms of twinning-induced plasticity steels. Scripta Materialia 58, 484–487, doi:10.1016/j.scriptamat.2007.10.050 (2008).

45. Xi T et al. Copper precipitation behavior and mechanical properties of Cu-bearing 316L austenitic stainless steel: A comprehensive cross-correlation study. Materials Science and Engineering: A 675, 243–252, doi:10.1016/j.msea.2016.08.058 (2016).

46. Zhang J-S High temperature deformation and fracture of materials. (Elsevier, 2010).
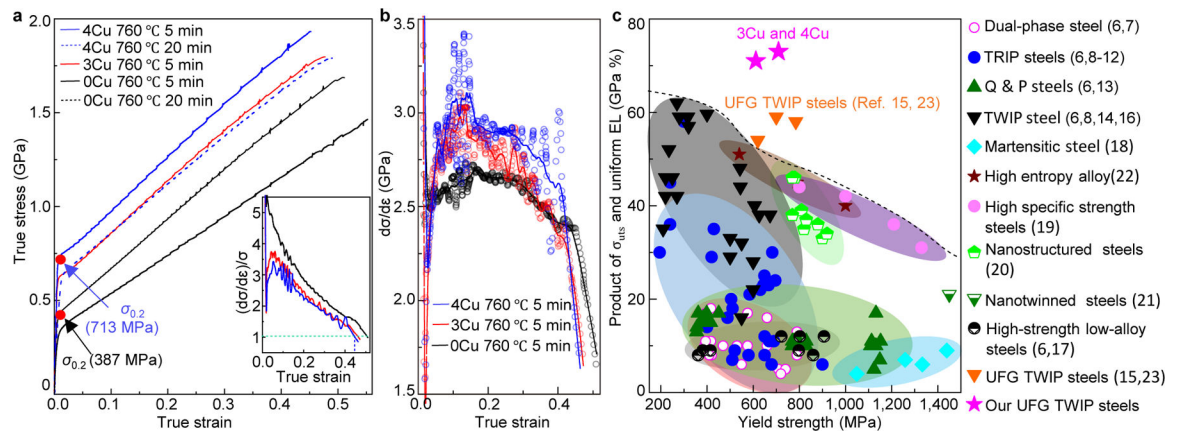
Figure 1. Mechanical properties.

a, Room-temperature tensile stress-strain curves of 0Cu, 3Cu and 4Cu annealed for 5 and 20 min at 760 °C. Yield strengths are highlighted by red solid circles. The inset is the corresponding normalized strain hardening response $((d\sigma/d\varepsilon)/\sigma)$ of 0Cu, 3Cu and 4Cu annealed for 5 min at 760°C. **b,**. Strain hardening response $(d\sigma/d\varepsilon)$ of 0Cu, 3Cu and 4Cu annealed for 5 min at 760°C. **c,** Yield strength versus the product of σ_{uts} and uniform EL of 3Cu and 4Cu annealed at 760°C for 5min, respectively, as compared with those of other high performance materials reported in literature[6–23].
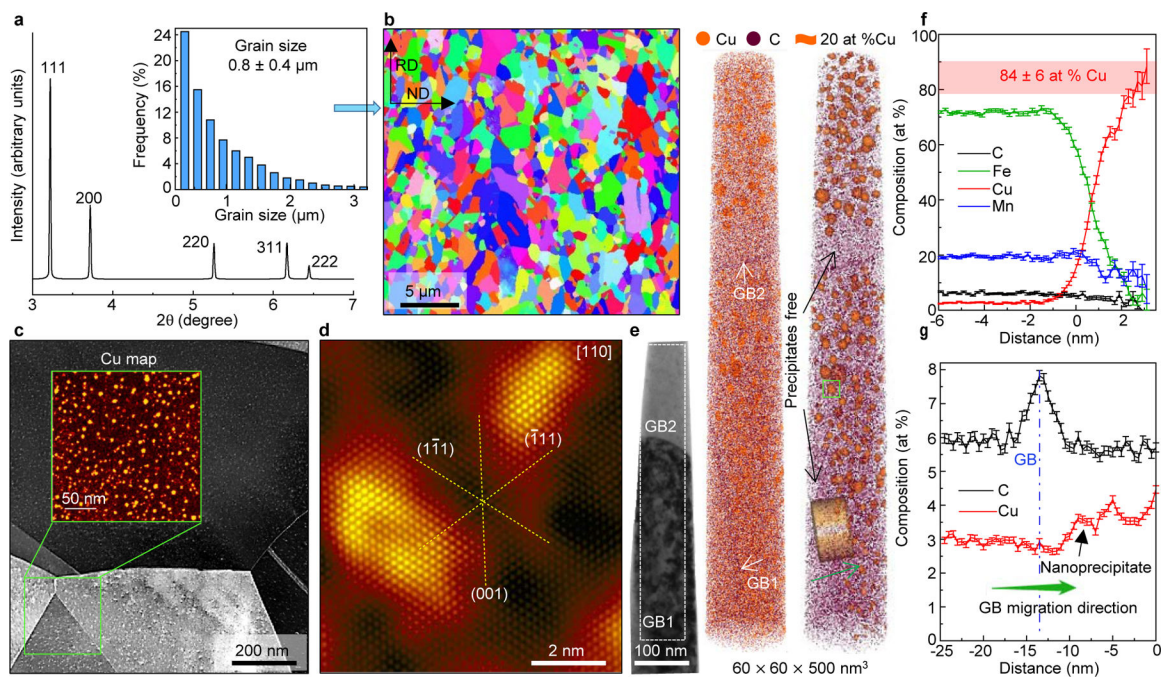
Figure 2. Microstructure characterization of 4Cu annealed at 760 °C for 5 min.
a, b, Synchrotron high-energy XRD pattern and EBSD map showing a single fcc phase with a ultrafine structure. The inset in **a** is the grain size distribution. RD indicates the rolling direction while ND stands for the normal direction. **c,** ADF-STEM image displaying a high density of intragranular nanoprecipitates (bright particles).The inset is the STEM EDS-SI image from the marked region. **d,** Atomic resolution ADF-STEM image demonstrating the fully coherent disordered nature of Cu-rich nanoprecipitates. **e,** Correlated TEM and atom probe analysis across two grain boundaries (GB) presenting the size, morphology and spatial distribution of Cu-rich nanoprecipitates. **f,** Proximity histogram showing the composition change across one nanoprecipitate (marked by the green square). **g,** 1D concentration profile of cylindrical region showing no apparent elemental segregation at grain boundary. The error bars are standard deviations of the mean while the isoconcentration surface is 20 at % Cu.
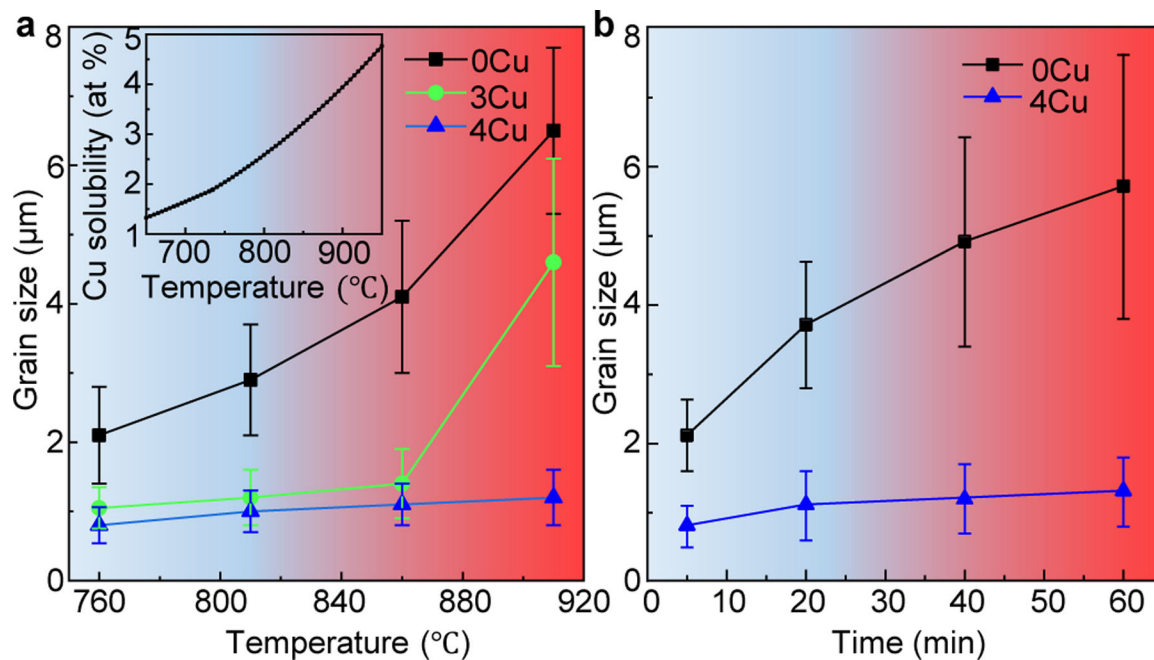
**Figure 3. Effects of annealing temperature and time on the UFG structure.**
a, Evolution of grain size of 0Cu, 3Cu and 4Cu after annealing at 760, 810, 860 and 910 °C for 5 min. The inset is the calculated equilibrium Cu solubility in the matrix over a temperatre range of 650 to 950 °C. **b**, Evolution of grain size of 0Cu and 4Cu as a function of annealing time from 5 to 60 min at 760 °C. The 4Cu exhibits the most stable UFG structure, indicating a broad thermomechanical processing window. The error bars represent the width of grain size distribution.
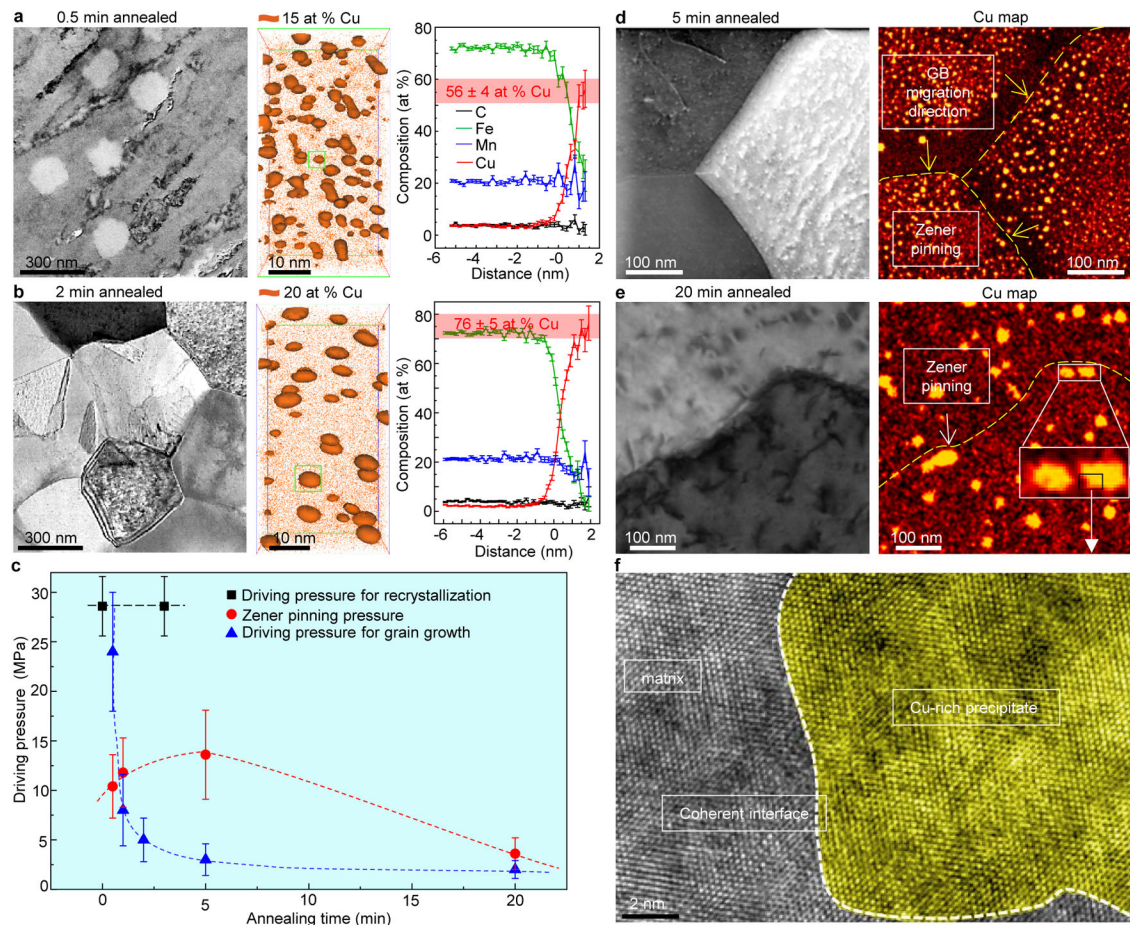
Figure 4. Mechanisms for effective grain refinement and high thermal stability.
a, b, ABF-STEM images, 3D reconstructions of APT data and the corresponding proximity histograms across two precipitates (marked by the blue squares) of the 4Cu annealed at 760 °C for 0.5 and 2 min, respectively, showing the development of recrystallization and nanoprecipitation with annealing time. **c**, Evolution of driving pressure for recrystallization, driving pressure for grain growth and Zener pinning pressure as a function of annealing time. **d**, **e**, ABF-STEM images and their corresponding STEM EDS-SI images of the 4Cu annealed at 760 °C for 5 and 20 min, respectively, demonstrating the evidence of Zener pinning. **f,** HR-TEM image of one nanoprecipitate at a grain boundary showing a coherent interface with the shrinking grain. The error bars are standard deviations of the mean. The isoconcentration surfaces in **a** and **b** are 15 at % and 20 at % Cu, respectively.
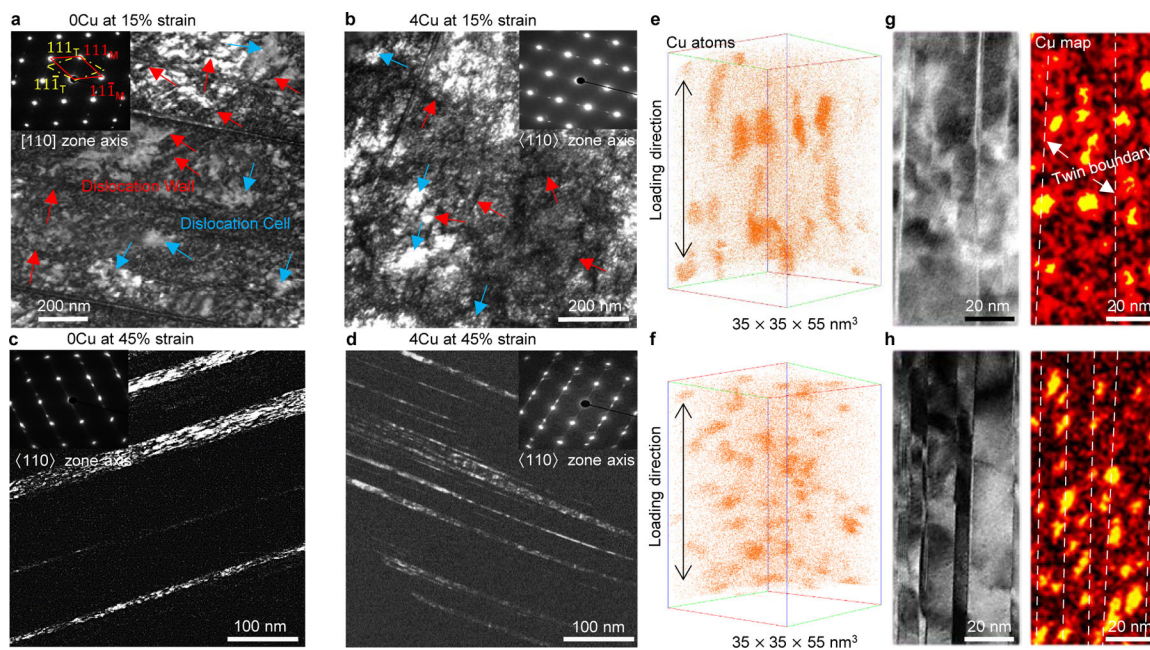
Fig.5. Deformed microstructure of UFG 0Cu and 4Cu.
a, **b**, Bight-field TEM images of UFG 0Cu and 4Cu pre-strained to 15 %, respectively, revealing dense dislocation walls (red arrows), dislocation cells (blue arrows) and nanotwins with interspacing of 300–500 nm in both alloys. **c**, **d**, Dark-field TEM images of 0Cu and 4Cu pre-strained to 45 %, respectively. The insets show the corresponding SAED patterns. **e**, **f**, **g**, **h**, APT reconstructions and ADF-STEM images with the corresponding STEM EDS-SI images of 4Cu pre-strained to 15 % and 45 %, respectively, showing development of nanoprecipitates with strain and their interaction with nanotwins.